Meccanica
DOI 10.1007/s11012-011-9500-7

Stress intensity factors for surface cracks in round bar under single and combined loadings

A.E. Ismail · A.K. Ariffin · S. Abdullah · M.J. Ghazali

Received: 27 September 2010 / Accepted: 10 October 2011

Abstract This paper numerically discusses stress intensity factor (SIF) calculations for surface cracks in round bars subjected to single and combined loadings. Different crack aspect ratios, a/b, ranging from 0.0 to 1.2 and the relative crack depth, a/D, in the range of 0.1 to 0.6 are considered. Since the torsion loading is non-symmetrical, the whole finite element model has been constructed, and the loadings have been remotely applied to the model. The equivalent SIF, F^*_{EQ} is then used to combine the individual SIF from the bending or tension with torsion loadings. Then, it is compared with the combined SIF, F^*_{FE} obtained numerically using the finite element analysis under similar loadings. It is found that the equivalent SIF method successfully predicts the combined SIF, F^*_{EQ} for Mode I when compared with F^*_{FE}. However, some discrepancies between the results, determined from the two different approaches, occur when F_{III} is involved. Meanwhile, it is also noted that the F^*_{FE} is higher than the F^*_{EQ} due to the difference in crack face interactions and deformations.

Keywords Combined stress intensity factors · Finite element analysis · Surface crack · Crack face interactions

1 Introduction

Mechanical power transmission is successfully conducted by the application of the cylindrical-shaped bar. This transmission is not only subjected by single loading, but it is frequently occurred in combined loadings. Such structural components are subjected to cyclic stresses which can cause mechanical damages and premature failure. In services, a rotating shaft can generally be subjected to combined loading due to its self-weight, which induces a bending moment, and sometime it is combined with bending and/or axial stresses. Many factors have been contributed for surface cracks to initiate such as notches [1–3], corrosion [4] and metallurgical [5] defects. In fact, any arbitrary shapes of crack initiation may grow and take a semi-elliptical shape [6]. Then, linear elastic fracture mechanics (LEFM) has been used to analyse stress intensity factors (SIFs) along the crack front.

The solution of SIFs for a wide range of geometries under Mode I loadings has been reported elsewhere in the literature [7–9]. However, the SIFs under Mode III [10] and under combined loadings such

A.E. Ismail (✉)
Department Engineering Mechanics, Faculty of Mechanical & Manufacturing Engineering, University Tun Hussein Onn Malaysia, 86400 Batu Pahat, Johor, Malaysia
e-mail: emran@uthm.edu.my

A.K. Ariffin · S. Abdullah · M.J. Ghazali
Department Mechanical & Materials Engineering, Faculty of Engineering & Built Environment, University Kebangsaan Malaysia, 43600 UKM Bangi, Selangor, Malaysia

Published online: 08 November 2011

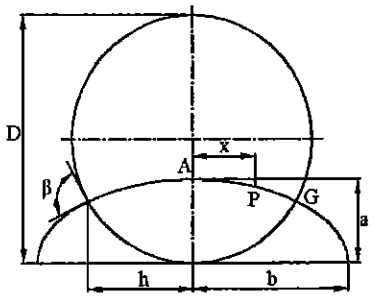

Fig. 1 Arbitrary crack shape [9]

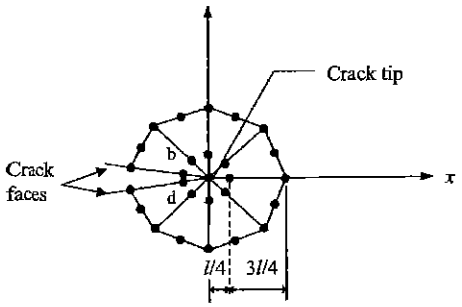

Fig. 2 Singular element around the crack tip

as bending or tension and torsion are rarely studied [11–17]. Therefore, the aim of this study is to obtain the SIFs for semi-elliptical surface cracks subjected to bending, tension, torsion and the combination of such loadings. This numerical work is also carried out to investigate whether the SIFs from different modes could be explicitly combined and then compared to the ones using the finite element analysis. Finally, the discrepancies between the two methods are discussed in terms of mesh deformation by suggesting such discrepancies seem to depend on the crack face interaction.

2 Evaluation of fracture parameters

2.1 Stress intensity factors

The finite element method is an appropriate approach to calculate the stress intensity factor (SIF) for linear elastic fracture mechanics problems. In order to determine the SIFs, a displacement extrapolation method [18] is used in this study. Several other works have implemented a similar method are also available [19, 20]. In order to analyse the cracks, it is frequently modelled as a semi-elliptical crack shape. This due to the fact, any arbitrary crack shapes will grow to take semi-elliptical crack geometry [6]. Figure 1 shows an arbitrary crack shape where the crack face is parallel to the x-axis and the z-axis is normal to the x–y plane. While, Fig. 2 shows an arrangement of singular finite elements around a crack tip used in this work.

After obtaining the elastic finite element solution of the particular problem, nodal displacements between two crack faces are determined and used to compute the SIFs as follows

$$K_I = \frac{2G\sqrt{2\pi}}{1+\kappa}\frac{|v_b - v_d|}{\sqrt{r}} = \frac{2G\sqrt{2\pi}}{1+\kappa}\frac{|\Delta v|}{\sqrt{r}} \tag{1}$$

$$K_{II} = \frac{2G\sqrt{2\pi}}{1+\kappa}\frac{|u_b - u_d|}{\sqrt{r}} = \frac{2G\sqrt{2\pi}}{1+\kappa}\frac{|\Delta u|}{\sqrt{r}} \tag{2}$$

$$K_{III} = 2G\sqrt{2\pi}\frac{|w_b - w_d|}{\sqrt{r}} = 2G\sqrt{2\pi}\frac{|\Delta w|}{\sqrt{r}} \tag{3}$$

where, K_I, K_{II} and K_{III} are the respective mode I, II and III SIFs, Δv, Δu and Δw are the relative nodal displacements between two crack faces in the direction of y-axis, x-axis and z-axis, respectively, and G is the modulus of rigidity. For plain strain condition, $\kappa = 3 - 4\upsilon$, where, υ is the Poisson's ratio. All the SIFs obtained from the analysis are converted into normalised values in order to ensure the generality of the results. A normalised SIF, F, can be defined as follows [11]

$$F_{I,a} = \frac{K_{I,a}}{\sigma_a\sqrt{\pi a}} \tag{4}$$

$$F_{I,b} = \frac{K_{I,b}}{\sigma_b\sqrt{\pi a}} \tag{5}$$

$$F_{II} = \frac{K_{II}}{\tau_{xy}\sqrt{\pi a}} \tag{6}$$

$$F_{III} = \frac{K_{III}}{\tau_{xy}\sqrt{\pi a}} \tag{7}$$

where, σ_a, σ_b and τ_{xy} are the axial, bending and shear stresses, respectively and a is a crack depth.

2.2 J-integral

The concepts of SIFs are successfully used as a driving fracture parameter within the scope of linear elastic analysis. However, the application of this parameter breakdown when large amount of plastic deformation induced during loadings especially for the

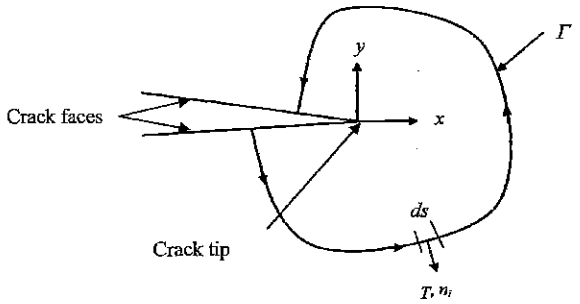

Fig. 3 A definition of contour path to evaluate J-integral

high strength and low toughness materials is involved. Therefore, J-integral is used instead of SIF as a driving fracture parameter. It is firstly introduced by assuming a crack in two-dimensional plate [21], J-integral is defined as a contour, Γ around the crack tip. It is evaluated counter-clockwise as depicted in Fig. 3 and can be expressed as

$$J = \int_{\Gamma} \left(W dy - T \cdot \frac{\partial u}{\partial z} ds \right) \tag{8}$$

where, T is a outward traction vector along the contour, Γ is defined as $T_i = \sigma_{ij} n_i$ or it is a force per unit length, u is a displacement vector and ds is an element on the contour, Γ. While, W is a strain energy density expressed as

$$W = \int_0^{\varepsilon} \sigma_{ij} d\varepsilon_{ij} = \int_0^{\varepsilon} \{\sigma\}^T d\{\varepsilon\} \tag{9}$$

where, ε_{ij} is a strain tensor and $\{\varepsilon\}$ represents as a strain vector. In elastic-plastic analysis J-integral is composed of two parts, elastic J-integral, J_e and plastic J-integral, J_p as follows [22]

$$J = J_e + J_p \tag{10}$$

where J_e can be obtained numerically using finite element method or by the following expression [23]

$$J_e = \frac{K_I^2}{\kappa} \tag{11}$$

where, K is the SIF, $\kappa = E$ for plane stress and $\kappa = E/(1 - \upsilon^2)$ for plane strain.

3 Finite element modelling

The geometry of the crack shown in Fig. 1 can be described by the dimensionless parameters a/D and

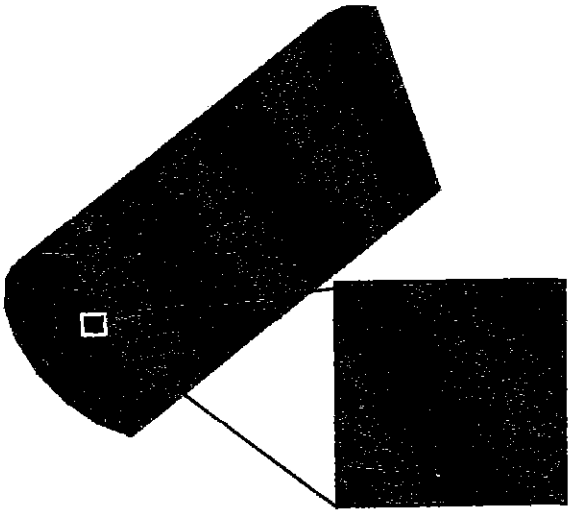

Fig. 4 A quarter finite element model with an associated crack tip singular element

a/b, the so-called relative crack depth and crack aspect ratio, respectively, where D, a and b are the diameter of the bar, the crack depth and the major diameter of the ellipse. In this work, a/b is ranging between 0.0 to 1.2 [12–14], while, a/D is in the range of 0.1 to 0.6 [12–14] which are based on the experimental observations [4, 6, 12]. Any arbitrary point, P on the crack front can also be normalised through the ratio x/h, where h is the crack width, and x is the arbitrary distance of P. The outer diameter of the cylinder is 50 mm and the total length is 200 mm.

A finite element model is developed using ANSYS [24], and a special attention is paid to the crack tip by employing 20-node iso-parametric quadratic brick elements. The square-root singularity of stresses and strains is modelled by shifting the mid-point nodes to the quarter-point locations around the crack-tip region. A quarter finite element model is shown in Fig. 4. In order to remotely apply loadings on the structural component, a rigid element or multi-point constraint (MPC) is used to connect the nodes at a circumferential line at the end of the component to an independent node. Figure 5 shows a technique of constructing the independent node connected to the model using a rigid beam element. The bending moment, M_y, and the torsion moment, T_x, are directly applied to this node, whereas the axial force, F is directly applied to the direction-x on the cross-sectional area of the round bar. At the other end, the component is fully constrained in all degrees of freedom. For combined

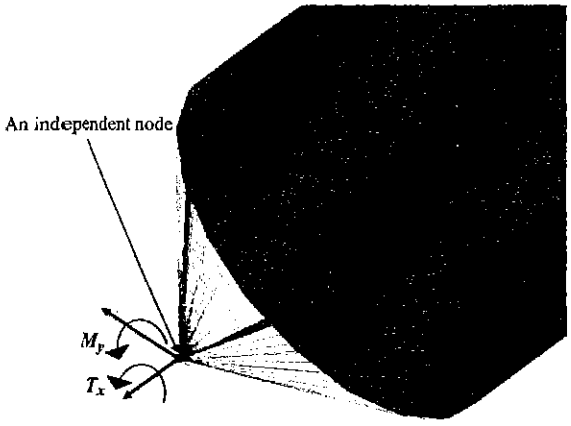

Fig. 5 Remotely applied loadings on the model

loadings, two types of loading ratios are used, which are defined as follows:

$$\vartheta = \frac{\sigma_b}{\sigma_a} \tag{12}$$

$$\lambda = \frac{\tau_{xy}}{\sigma_x} \tag{13}$$

where ϑ is the loading ratio between the bending stress, σ_b, and the axial stress, σ_a, and λ is the ratio between the shear stress, τ_{xy}, and the bending or axial stresses, σ_x. The ratios for both (12) and (13) are 0.5, 1.0 and 2.0.

In order to obtain a suitable finite element model, it is needed to compare the proposed model with others available in the literature [12–14]. Figure 6 shows a comparison of the dimensionless SIFs under bending and tension loadings. Two crack aspect ratio, a/b used for the validation purposes, namely 0.0 and 1.0. It has been found that the findings of this study are in agreement with those determined by the previous models where the curves have coincident to each others. The solution of Mode III SIFs is difficult to obtain [11, 15, 25] and consequently compare with the present results. Therefore, it can be assumed that the present model is also suitable to analyse Mode III condition in a satisfactory way.

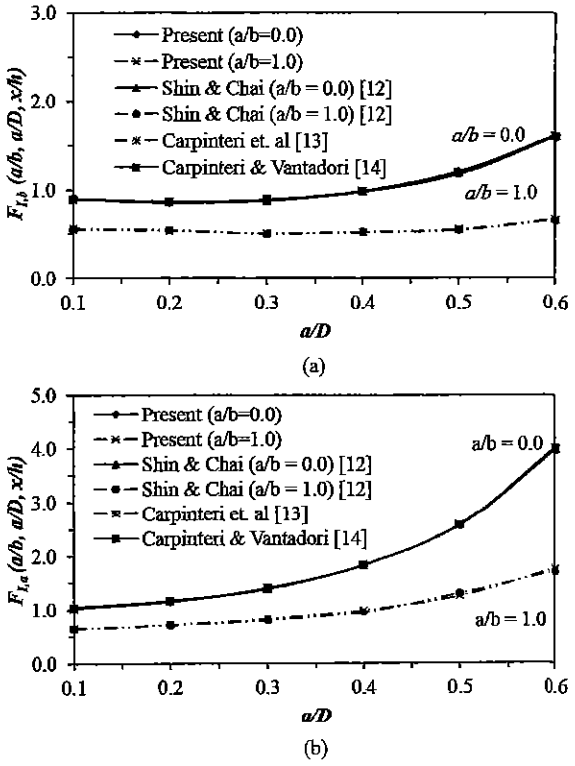

Fig. 6 Finite element model validations under (**a**) bending and (**b**) tension stresses

4 Results and discussion

4.1 Stress intensity factors under single loading conditions

Figures 7 to 10 show the results observed along the crack front for several crack conditions that are subjected by tension force, bending moment, and torsion moment. The SIFs are calculated at seven points along the crack front. However, the SIF at the intersection, between the crack and the surface, is not determined due to the square-root singularity problem. Consequently, the use of a quarter point finite element does not produce reliable results in the outer intersection surface.

Figures 7(a) and 7(b) show the variations of $F_{I,a}$ along the crack front under tension stress for two crack aspect ratios, $a/b = 0.4$ and 1.2, respectively. As for $a/b = 0.4$, the SIF is uniformly distributed along the crack front. When the x/h approached the outer surface of the bar, $F_{I,a}$ is found to be slightly higher than the others. Therefore, the maximum $F_{I,a}$ always occurs at the intersection area. Under tension stress, the crack growth starts at the intersection point, and the semi-elliptical crack front is flattened as the cracks grows [6, 13, 15]. For the case of $a/b = 1.2$, the parameter $F_{I,a}$ is affected just a little by a/D, particularly when $a/D \leq 0.3$. For $x/h \geq 0.6$, $F_{I,a}$ curves diverge and the maximum values for each curve are

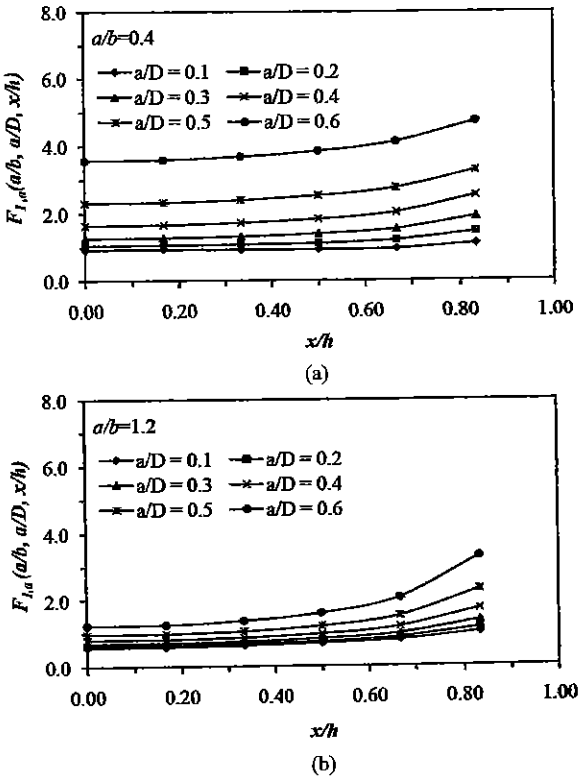

Fig. 7 The variations of $F_{I,a}$ along the crack front for **(a)** $a/b = 0.4$ and **(b)** $a/b = 1.2$

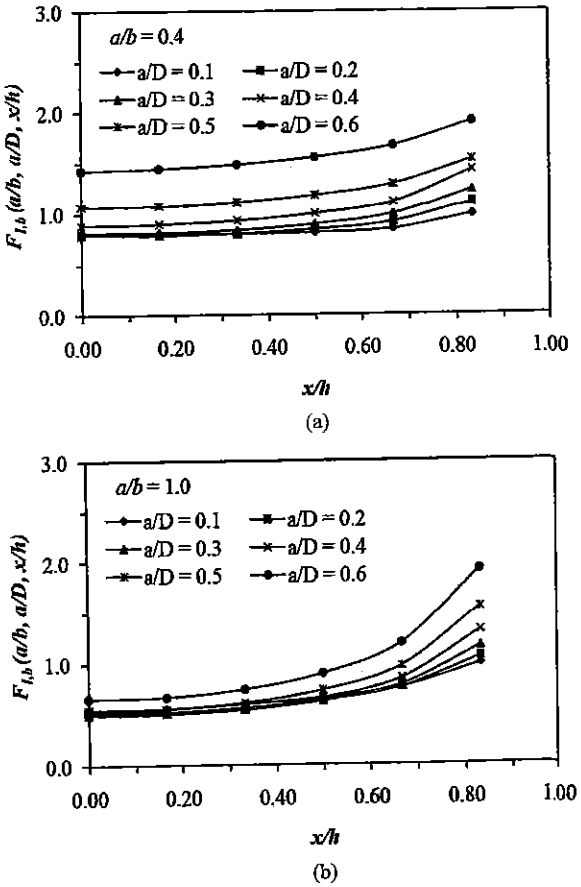

Fig. 8 The variations of $F_{I,b}$ along the crack front for **(a)** $a/b = 0.4$ and **(b)** $a/b = 1.0$

attained. The detail of $F_{I,a}$ can be found elsewhere [9, 11, 12, 16].

The SIFs under bending moment is shown in Fig. 8. Since the curves of $F_{I,b}$ is almost identical to each other except the curves are closer to each other when a/b is increased. Therefore the case of $a/b = 0.4$ and 1.0 are considered. However, $F_{I,b}$ is lower than $F_{I,a}$ due to the different in crack faces opening mechanisms. For the case of $a/D \leq 0.3$ in the range of $x/h < 0.5$, $F_{I,b}$ is not significantly affected by a/D and x/h. This is probably due to crack closure occurred around the crack front which is not to occur for the relatively deeper cracks ($a/b > 0.3$). The detail of $F_{I,b}$ can be found elsewhere [9, 11, 12, 16].

The SIFs determined using torsion moment not only produced F_{III} but it is also induced F_{II} due to out-of-plane of crack deformation. Figure 9 shows the F_{II} under such loading. Referring Fig. 9(a), F_{II} at the deepest point of the crack front ($x/h = 0.0$) is equal to zero. Then, F_{II} increases by moving towards the intersection point between the crack front and the outer surface of the round bar. No significant curve fluctuations can be observed along the crack front when a/D is increased. However, F_{II} diverged when $x/h > 0.6$ where the deeper cracks attain the higher F_{II}. Similar trend of F_{II} can be observed when higher value of a/b is used as it can be seen in Fig. 9(b).

Figure 10 shows F_{III} along the crack front, in the case of torsion loading. The behaviour of F_{III} is strongly related to the value of the relative crack depth, a/D. For $a/D < 0.3$, the maximum F_{III} occurs at the deepest point of the crack front. For $a/D > 0.3$, the maximum F_{III} is shifted at the outer surface. The curve of $a/D = 0.3$ is not affected by x/h where insignificant curve fluctuation can be observed. Figure 10(a) shows the F_{III} along the crack front for $a/b = 0.4$. It is clearly seen that the interchanging point of maximum and minimum F_{III} occurred at $x/h = 0.3$. However, when a/b is increased to $a/b = 1.0$, this point has moved to $x/h \approx 0.6$ as in Fig. 10(b). This movement of x/h has clearly affected the distributions of

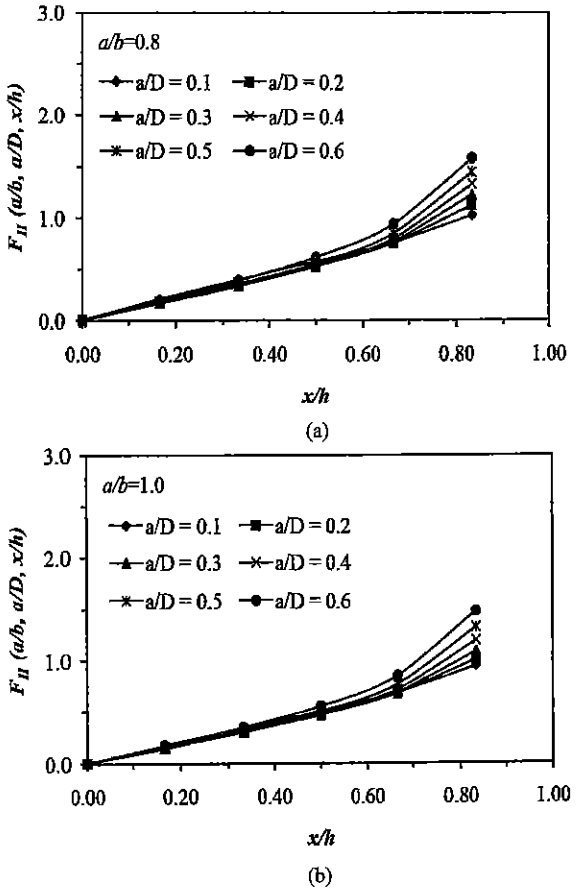

Fig. 9 The variations of F_{II} along the crack front for (**a**) $a/b = 0.8$ and (**b**) $a/b = 1.0$

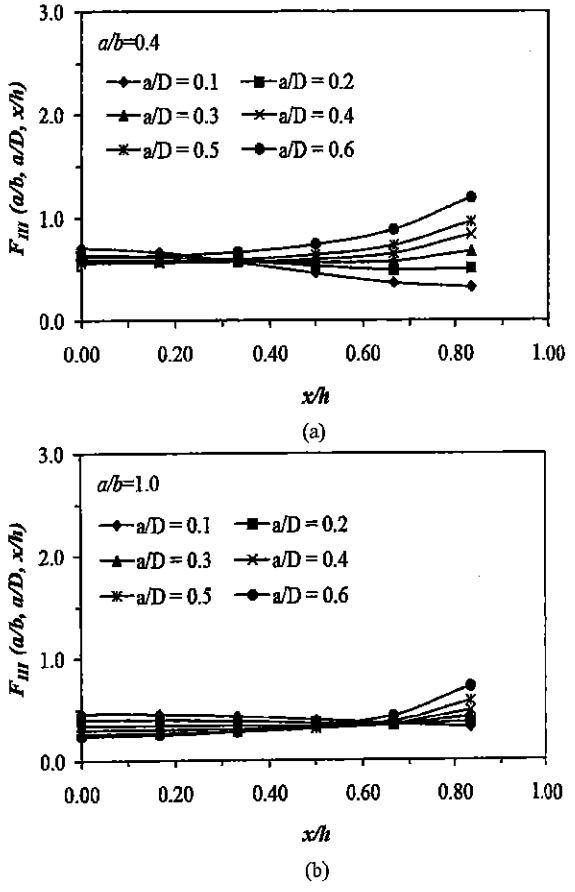

Fig. 10 The variations of F_{III} along the crack front for (**a**) $a/b = 0.4$ and (**b**) $a/b = 1.0$

F_{III} along the crack front where the F_{III} has been reduced. This is due to the fact that deeper cracks at $a/b = 1.0$ capable to increase the integrity of the bar subjected to torsion moments. Tables 1 and 2 list all the F_{II} and F_{III} SIFs obtained under pure torsion.

4.2 Stress intensity factors under combined loadings

In previous studies [11, 15], it is hard to find the SIFs under combined loadings. This is because it was assumed that combined SIFs could be obtained using a superposition technique. This assumption is established for a similar type of loading mode, for example mode I [7]. The normalised SIFs under combined loading, F^*_{EQ}, under mode I loadings are here obtained by the superposition method defined as

$$F^*_{EQ} = F_{I,a} + \vartheta F_{I,b} \tag{14}$$

where ϑ is the stress ratio defined in (12). Then, these combined SIFs are compared with the combined SIFs, F^*_{FEA}, obtained numerically using finite element analysis, with an excellent agreement as shown in Fig. 11.

Further enhancement of the superposition technique is required to include F_{II} and F_{III}. Therefore, the equivalent SIF method [26] is used instead of a superposition method. The equivalent SIF is defined as the following expression

$$K_{eqv} = \sqrt{K_I^2 + K_{II}^2 + \frac{K_{III}^2}{1-\nu}} \tag{15}$$

where, K_{eqv} is the equivalent SIF and υ is the Poisson's ratio. It is assumed that $K_{eqv} = K^*$ where K^* is a combined SIF. Substituting (4) or (5), (6) and (7) into (15) yields the following expression

$$K^* = \left((F_{I,x}\sigma_x\sqrt{\pi a})^2 + (F_{II}\tau_{xy}\sqrt{\pi a})^2 + \left(\frac{F_{III}\tau_{xy}\sqrt{\pi a}}{1-\nu}\right)^2 \right)^{1/2} \tag{16}$$

Table 1 Normalised mode II stress intensity factors, F_{II} under torsion loading

x/h	a/D	a/b						
		0.0	0.2	0.4	0.6	0.8	1.0	1.2
0.0	0.1	0.0022	0.0016	0.0010	0.0014	0.0012	0.0012	0.0005
	0.2	0.0014	0.0013	0.0013	0.0012	0.0011	0.0011	0.0010
	0.3	0.0004	0.0054	0.0000	0.0001	0.0000	0.0008	0.0005
	0.4	0.0018	0.0015	0.0015	0.0014	0.0013	0.0012	0.0011
	0.5	0.0031	0.0027	0.0027	0.0027	0.0026	0.0024	0.0021
	0.6	0.0031	0.0027	0.0028	0.0029	0.0028	0.0027	0.0024
0.17	0.1	0.3580	0.3464	0.3253	0.2586	0.2048	0.1675	0.1412
	0.2	0.2507	0.2456	0.2380	0.2123	0.1798	0.1529	0.1321
	0.3	0.2175	0.2053	0.2051	0.1884	0.1663	0.1455	0.1280
	0.4	0.2091	0.2057	0.1967	0.1813	0.1628	0.1448	0.1288
	0.5	0.2179	0.2140	0.2041	0.1877	0.1693	0.1517	0.1353
	0.6	0.2431	0.2415	0.2289	0.3127	0.1891	0.1684	0.1495
0.33	0.1	0.6450	0.6277	0.5832	0.4832	0.3964	0.3340	0.2874
	0.2	0.4943	0.4854	0.4674	0.4185	0.3582	0.3092	0.2705
	0.3	0.4389	0.4145	0.4161	0.3816	0.3372	0.2967	0.2627
	0.4	0.4251	0.5001	0.4035	0.4890	0.3333	0.2967	0.2645
	0.5	0.4429	0.4365	0.4172	0.3846	0.3472	0.3110	0.2773
	0.6	0.4942	0.4906	0.4662	0.4280	0.3868	0.3446	0.3057
0.50	0.1	0.8540	0.8369	0.7706	0.6707	0.5740	0.5018	0.4445
	0.2	0.7323	0.7222	0.6913	0.6238	0.5412	0.4760	0.4243
	0.3	0.6758	0.6388	0.6470	0.5927	0.5253	0.4656	0.4161
	0.4	0.6646	0.6585	0.6400	0.5876	0.5289	0.4716	0.4218
	0.5	0.6940	0.6860	0.6589	0.6123	0.5546	0.4972	0.4437
	0.6	0.7721	0.7684	0.7343	0.6778	0.6149	0.5494	0.4880
0.67	0.1	1.0193	1.0076	0.9278	0.8532	0.7568	0.6834	0.6230
	0.2	0.9851	0.9752	0.8993	0.8610	0.7555	0.6745	0.6094
	0.3	0.9574	0.9122	0.9361	0.9760	0.7676	0.6827	0.6145
	0.4	0.9637	0.9560	0.9533	0.8788	0.7962	0.7104	0.6356
	0.5	1.0139	1.0013	0.9780	0.9253	0,8481	0.7623	0.6787
	0.6	1.1250	1.1174	1.0857	.0216	0.9384	0.8466	0.7525
0.83	0.1	1.2440	1.2542	1.1670	1.1407	1.0244	0.9415	0.8760
	0.2	1.3674	1.3563	1.3344	1.2754	1.1244	1.0054	0.9178
	0.3	1.4197	1.3801	1.4477	1.3648	1.2263	1.0865	1.1306
	0.4	1.4682	1.4621	1.5366	1.4366	1.3312	1.1906	1.0540
	0.5	1.5488	1.5402	1.5385	1.5172	1.4476	1.3212	1.1672
	0.6	1.7060	1.6959	1.6778	1.6438	1.5781	1.4808	1.3252

Table 2 Normalised mode III stress intensity factors, F_{III} under torsion loading

x/h	a/D	a/b						
		0.0	0.2	0.4	0.6	0.8	1.0	1.2
0.0	0.1	0.8093	0.7760	0.7088	0.6377	0.5338	0.4615	0.4025
	0.2	0.7196	0.6964	0.6380	0.5557	0.4700	0.3964	0.3379
	0.3	0.6672	0.5921	0.5918	0.5098	0.4192	0.3397	0.2779
	0.4	0.6435	0.6243	0.5679	0.4820	0.3824	0.2920	0.2234
	0.5	0.6533	0.6326	0.5711	0.4768	0.3629	0.2556	0.1745
	0.6	0.7118	0.6884	0.6177	0.5076	0.3707	0.2354	0.1320
0.17	0.1	0.7641	0.7331	0.6671	0.5929	0.5180	0.4526	0.3987
	0.2	0.7046	0.6819	0.6230	0.5432	0.4610	0.3910	0.3361
	0.3	0.6623	0.5870	0.5873	0.5053	0.4154	0.3373	0.2779
	0.4	0.6447	0.6255	0.5698	0.4831	0.3830	0.2926	0.2253
	0.5	0.6597	0.6389	0.5784	0.4831	0.3682	0.2598	0.1789
	0.6	0.7245	0.7029	0.6315	0.5203	0.3818	0.2449	0.1402
0.33	0.1	0.6554	0.6307	0.5696	0.5281	0.4760	0.4273	0.3861
	0.2	0.6648	0.6449	0.5850	0.5115	0.4377	0.3767	0.3307
	0.3	0.6499	0.5752	0.5779	0.4955	0.4068	0.3324	0.2787
	0.4	0.6499	0.6314	0.5782	0.4890	0.3872	0.2966	0.2322
	0.5	0.6802	0.6596	0.5998	0.5037	0.3856	0.2740	0.1927
	0.6	0.7635	0.7415	0.6705	0.5578	0.4152	0.2728	0.1638
0.50	0.1	0.5274	0.5114	0.4605	0.4484	0.4179	0.3881	0.3628
	0.2	0.6092	0.5936	0.5360	0.4714	0.4063	0.3557	0.3210
	0.3	0.6350	0.5629	0.5699	0.4871	0.3988	0.3277	0.2807
	0.4	0.6635	0.6463	0.5992	0.5061	0.4005	0.3077	0.2452
	0.5	0.7203	0.7001	0.6420	0.5452	0.4217	0.3026	0.2180
	0.6	0.8357	0.8129	0.7428	0.6277	0.4777	0.3243	0.2054
0.67	0.1	0.4070	0.4027	0.3699	0.3832	0.3653	0.3484	0.3358
	0.2	0.5495	0.5400	0.4945	0.4458	0.3869	0.3424	0.3150
	0.3	0.6283	0.5665	0.5810	0.5681	0.4128	0.3399	0.2944
	0.4	0.7009	0.6863	0.6563	0.5593	0.4482	0.3460	0.2784
	0.5	0.8014	0.7850	0.7330	0.6378	0.5063	0.3703	0.2728
	0.6	0.9712	0.9540	0.8858	0.7672	0.6062	0.4297	0.2873
0.83	0.1	0.3148	0.3326	0.3294	0.3549	0.3304	0.3153	0.3076
	0.2	0.5202	0.5214	0.5100	0.4866	0.4180	0.3651	0.3347
	0.3	0.6779	0.6464	0.6780	0.6145	0.5126	0.4184	0.3586
	0.4	0.8239	0.8178	0.8396	0.7427	0.6201	0.4851	0.3883
	0.5	0.9976	0.9938	0.9628	0.8903	0.7541	0.5777	0.4335
	0.6	1.2601	1.2537	1.1959	1.0952	0.9333	0.7181	0.5130

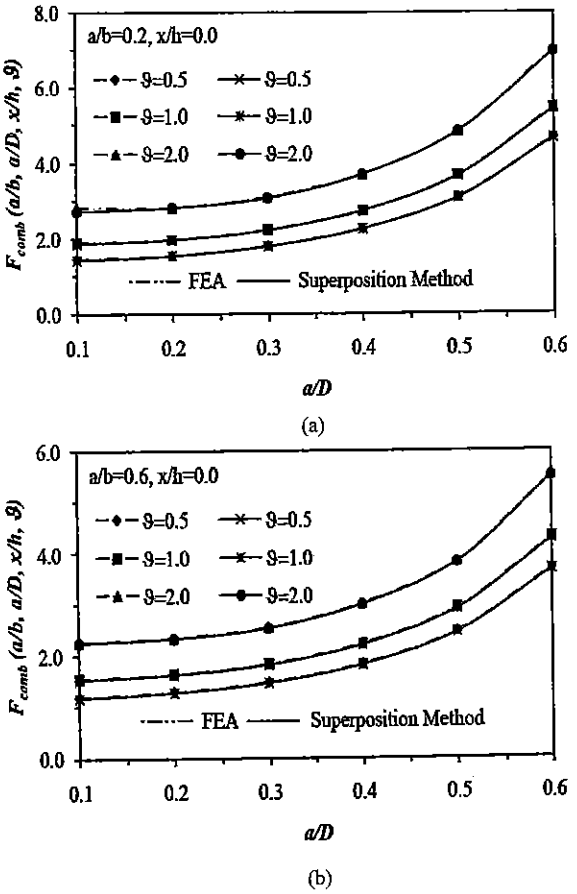

Fig. 11 Comparison between two methods (**a**) $a/b = 0.2$ and (**b**) $a/b = 0.6$

where σ_x can be represented as axial or bending stresses and $F_{I,x}$ can also be represented as the normalised SIF under bending or tension stress, respectively. Substituting (13) into (16), we obtain the following expression

$$K^* = \sqrt{(\sigma_x\sqrt{\pi a})^2\left[(F_{I,x})^2 + (\lambda F_{II})^2 + \left(\frac{\lambda F_{III}}{1-\nu}\right)^2\right]} \tag{17}$$

Rearranging (17) in terms of combined dimensionless SIF, F^* is given by

$$F^* = \frac{K^*}{\sigma_x\sqrt{\pi a}} = \sqrt{(F_{I,x})^2 + (\lambda F_{II})^2 + \left(\frac{\lambda F_{III}}{(1-\nu)}\right)^2} \tag{18}$$

Equation (18) can be divided into two separate equations given as

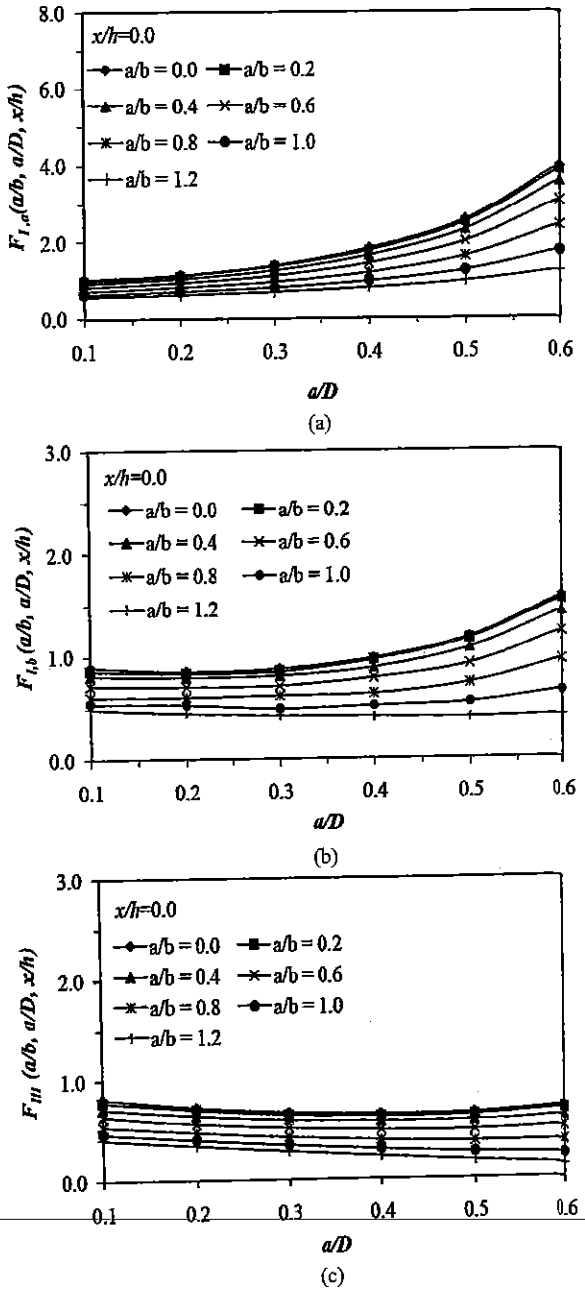

Fig. 12 Normalised SIFs at $x/h = 0.0$ for (**a**) $F_{I,a}$, (**b**) $F_{I,b}$ and (**c**) F_{III}

$$F^* = \frac{K^*_{FE}}{\sigma_x\sqrt{\pi a}} = F^*_{I,b\text{-}III,FE} \tag{19}$$

$$F^* = \sqrt{(F_{I,x})^2 + (\lambda F_{II})^2 + \left(\frac{\lambda F_{III}}{(1-\nu)}\right)^2} = F^*_{I,x\text{-}III,EQ} \tag{20}$$

where $F^*_{I,x\text{-}III,FE}$ is the normalised SIF obtained directly from finite element analysis under combined loadings, and $F^*_{I,x\text{-}III,EQ}$ is the normalised SIF obtained explicitly by combining the individual SIFs $F_{I,b}$, $F_{I,a}$, F_{II} and F_{III}. In order to simplify the analysis, the work focuses on this location at $x/h = 0.0$ where $F_{II} = 0.0$. Therefore, (20) can be then reduced to the following expression

$$F^*_{I,x\text{-}III,EQ} = \sqrt{(F_{I,x})^2 + \left(\frac{\lambda F_{III}}{(1-\nu)}\right)^2} \tag{21}$$

Figure 12 shows the SIFs obtained under single loading conditions at $x/h = 0.0$. It is indicated that, all the considered SIFs have decreased when a/b is increased and no significant effect on the SIFs for the relatively straight crack front ($a/b \leq 0.2$). For mode I conditions as shown in Figs. 12(a) and 12(b), the SIFs show the increasing trends as a/D increased especially under bending moment. Figure 12(c) on the other hand shows the SIFs under torsion moment obtained at $x/h = 0.0$. It is shown that lower values of F_{III} occurred when a/b is increased. This occurrence might be caused by the influence of crack geometries where deeper cracks are obtained using $a/b = 1.2$. These type of cracks attained fully constraint mechanisms around the crack front and producing lower F_{III} at $x/h = 0.0$.

It is hard to obtain a single value of SIF directly from ANSYS. Therefore, an elastic J-integral is used by assuming that a single value of J-integral under combined loading represented the unified SIFs consisting of K_I, K_{II} and K_{III}. This is because in ANSYS, if J-integral is used in the elastic or plastic regions, it calculates only a single value of J-integral even under combined loadings. The elastic J-integral, J_e, is as in (11) and it is rearranged in the terms of K and assuming that $K = K^*_{FE}$, where K^*_{FE} is a SIF under combined loadings obtained using finite element analysis, yields the following expression

$$K^*_{FE} = \sqrt{J_e\left(\frac{E}{1-\nu^2}\right)} \tag{22}$$

Equation (22) is used to convert the J-integral into the combined SIF for plain strain condition and it is substituted into (19). Then, $F_{I,a}$ or $F_{I,b}$ are combined explicitly with F_{III} through (21) using different stress ratio values, λ. The calculated F^*_{EQ} and F^*_{FE} are compared and the results are presented in Figs. 13 and 14.

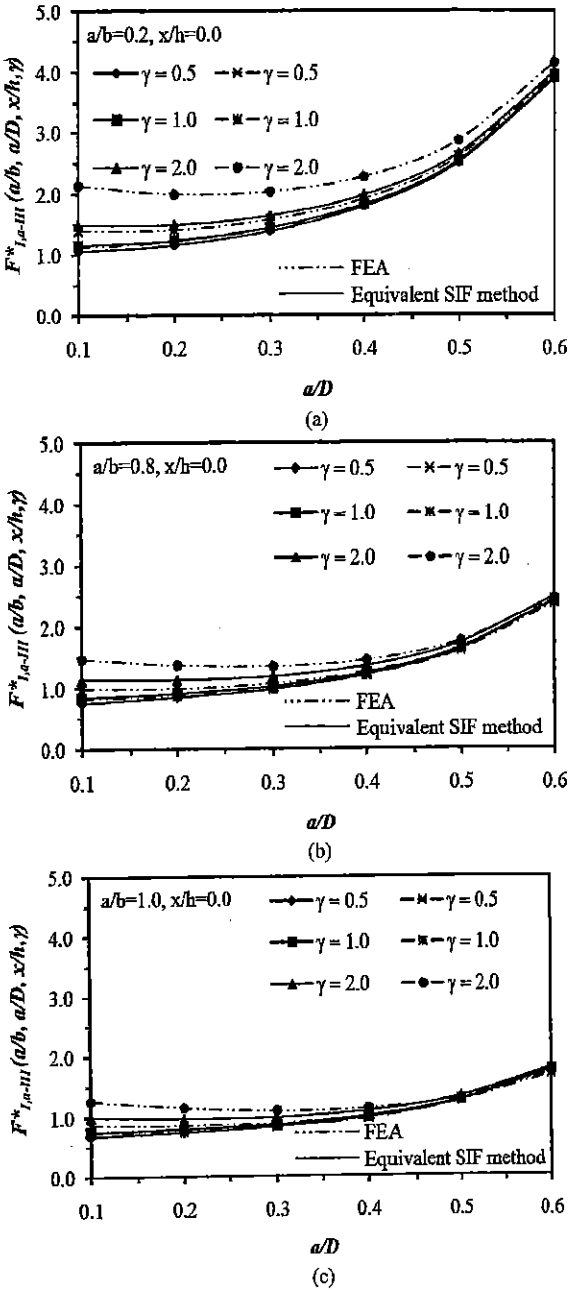

Fig. 13 Comparison of $F^*_{I,a\text{-}III}$ between two methods for (a) $a/b = 0.2$, (b) $a/b = 0.6$ and (c) $a/b = 1.0$ under combined tension and torsion loadings

Table 3 Normalised SIF under combined tension and torsion loadings, $F^*_{I,a\text{-}III,EQ}$ obtained using the equivalent SIF method

λ	a/D	a/b						
		0.0	0.2	0.4	0.6	0.8	1.0	1.2
0.5	0.1	1.0830	1.0436	0.9686	0.8718	0.7545	0.6704	0.6006
	0.2	1.0793	1.1548	1.0791	0.9678	0.8487	0.7301	0.6451
	0.3	1.0579	1.2948	1.2888	1.1425	0.9788	0.8260	0.7110
	0.4	1.0326	1.7893	1.6606	1.4532	1.2100	0.9852	0.8133
	0.5	1.0220	2.5116	2.3188	2.0102	1.6259	1.2563	0.9741
	0.6	1.0866	3.8779	3.5808	3.0743	2.4180	1.7558	1.2408
1.0	0.1	1.2281	1.1822	1.0934	0.9840	0.8457	0.7473	0.6661
	0.2	1.2099	1.2577	1.1717	1.0463	0.9129	0.7833	0.6889
	0.3	1.1573	1.3739	1.3566	1.1993	1.0238	0.8611	0.7383
	0.4	1.0994	1.8442	1.7096	1.4936	1.2406	1.0071	0.8289
	0.5	1.0627	2.5521	2.3546	2.0389	1.6465	1.2695	0.9820
	0.6	1.1097	3.9091	3.6080	3.0957	2.4325	1.7639	1.2444
2.0	0.1	1.6883	1.6222	1.4916	1.3422	1.1398	0.9975	0.8807
	0.2	1.6311	1.6049	1.4856	1.3144	1.1341	0.9672	0.8418
	0.3	1.4898	1.6530	1.5994	1.4039	1.1867	0.9888	0.8386
	0.4	1.3336	2.0493	1.8931	1.6452	1.3560	1.0904	0.8884
	0.5	1.2119	2.7080	2.4925	2.1501	1.7265	1.3212	1.0133
	0.6	1.1977	4.0314	3.7147	3.1798	2.4897	1.7958	1.2586

Figure 13 shows the plot of $F^*_{I,a\text{-}III}$ against a/D for different a/b subjected to combined tension and torsion loadings. It is indicated that the loading ratio, γ played an important role in determining the discrepancies among the results. Reducing these ratios from 2.0 to 1.0, the results are almost agreed to each other. The detail of $F^*_{I,a\text{-}III,EQ}$ and $F^*_{I,a\text{-}III,FE}$ are listed in Tables 3 and 4. Similar behaviour of combined SIFs under bending and torsion loadings, $F^*_{I,b\text{-}III}$ can be observed as shown in Fig. 14. However, the curves indicated that the significant influence of torsion loading on the combined SIFs especially for $a/b \geq 1.0$ where the curves have been reduced when a/D is increased. The detail of $F^*_{I,b\text{-}III,EQ}$ and $F^*_{I,b\text{-}III,FE}$ are listed in Tables 5 and 6.

The discrepancies of combined SIFs, F^* between the two approaches remarkably depend on the values of a/b, a/D and λ. For all cases of a/b, F^*_{EQ} is considerably in agreement with F^*_{FE} for all values of loading ratios except for $\lambda \geq 2.0$. When a/b increases, the discrepancies between the results obtained from the two different approaches are tremendously reduced, and all the F^* values then converge when deeper cracks are used.

4.3 Crack deformation mechanisms

Figures 15(a) and 15(b) include the deformed meshes of the cracks subjected to pure torsion and tension loadings, respectively. Note that, under pure torsion, the crack faces are completely closed, however under tension stress, the crack faces are opened. The situation in Fig. 15(c) is then produced using the FEA subjected to combined loading. In comparison with combined loadings, the crack faces are opened even the bar is subjected to torsion loading, implicating that such a mechanism is responsible to produce the discrepancies among the obtained results using the two different methods shown in Figs. 13 and 14. Similar trend of the crack behaviour can be observed under bending moment shown in Fig. 16. However, the cracks are not opened as wide as the cracks subjected to tension loadings.

Table 4 Normalised SIF under combined tension and torsion loadings, $F^*_{I,a\text{-}III,FE}$ obtained using finite element analysis

λ	a/D	a/b						
		0.0	0.2	0.4	0.6	0.8	1.0	1.2
0.5	0.1	1.0892	1.0495	0.9797	0.8776	0.8417	0.7505	0.6745
	0.2	1.1881	1.1569	1.0810	1.0188	0.8911	0.7773	0.6900
	0.3	1.4207	1.3850	1.2793	1.1798	1.0091	0.8558	0.7392
	0.4	1.8433	1.7904	1.6609	1.4531	1.2111	0.9886	0.8192
	0.5	2.5776	2.5106	2.3270	2.0129	1.6336	1.2658	0.9852
	0.6	3.9949	3.8905	3.5969	3.0944	2.4471	1.7796	1.2644
1.0	0.1	1.1965	1.1487	1.0789	0.9629	1.0701	0.9446	0.8477
	0.2	1.2619	1.2280	1.1616	1.2364	1.0723	0.9273	0.8316
	0.3	1.4764	1.4408	1.3449	1.3520	1.1495	0.9691	0.8329
	0.4	1.8837	1.8290	1.7158	1.4998	1.2512	1.0193	0.8426
	0.5	2.6113	2.5410	2.3736	2.0547	1.6681	1.2917	1.0041
	0.6	4.0195	3.9134	3.6421	3.1355	2.4812	1.8071	1.2832
2.0	0.1	1.5308	1.4834	1.3782	1.6213	1.6854	1.4841	1.3187
	0.2	1.5280	1.4867	1.3995	1.6406	1.5857	1.3591	1.1999
	0.3	1.6859	1.6387	1.5294	1.6534	1.5615	1.3081	1.1166
	0.4	2.0441	1.9857	1.8557	1.6178	1.5404	1.2920	0.9967
	0.5	2.7320	2.6588	2.4799	2.1426	1.7362	1.3409	1.0397
	0.6	4.1152	4.0055	3.7241	3.2020	2.5307	1.8349	1.3056

In the finite element analysis, the SIFs are calculated by referring to the relative distance between the two nodes situated on the crack faces. Then the SIFs obtained under torsion and tension loadings, F^*_{EQ} are explicitly combined through (21) and then compared with the SIFs determined numerically under combined loadings, F^*_{FE}. Under combined loading conditions, F^*_{FE} is found to be greater than F^*_{EQ} as shown in Fig. 13 due to the fact that longer relative node distances are produced when tension stress involved. Therefore, ANSYS calculated greater F_{III} compared with the F_{III} obtained under complete closed crack faces in the case of pure torsion loading.

On the other hand, Fig. 17 shows the condition of the bar under combined bending and torsion moments. It is also shown that the non-symmetrical stress distributions around the crack tip which is supported the construction of full finite element model. The discrepancies of SIFs are shown in Fig. 14 where the SIFs combined explicitly are lower than the SIFs obtained numerically. The discrepancies are caused due to the different in crack interactions as mentioned previously for the case of combined tension and torsion loadings.

5 Conclusion

Finite element analyses have been performed for semi-elliptical surface cracks in round bars under different and combined loadings. According to the literature reading, no solutions have been found to calculate the normalised SIFs under combined loadings are available. It has been assumed that the SIFs could be explicitly combined together. Based on the findings of the present study, the direct SIF combinations are concluded to be rather questionable and inappropriate when different modes of failure are involved. Further, the discrepancies of the results between the explicitly combined SIFs, F^*_{EQ} and the SIFs obtained numerically, F^*_{FE} are due to the different mechanisms shown by the deformed meshes, in which the crack faces are

Table 5 Normalised SIF under combined bending and torsion loadings, $F^{*}_{I,b\text{-}III,EQ}$ obtained using the equivalent SIF method

λ	a/D	a/b						
		0.0	0.2	0.4	0.6	0.8	1.0	1.2
0.5	0.1	0.9548	0.9195	0.8655	0.7633	0.6452	0.5763	0.5184
	0.2	0.9093	0.8699	0.8396	0.7401	0.6352	0.5550	0.4703
	0.3	0.9194	0.8928	0.8489	0.7428	0.6329	0.5223	0.4362
	0.4	1.0005	0.9955	0.9176	0.8120	0.6547	0.5326	0.4170
	0.5	1.1889	1.1912	1.0993	0.9397	0.7514	0.5587	0.4018
	0.6	1.5818	1.5751	1.4519	1.2484	0.9688	0.6652	0.4156
1.0	0.1	1.1167	1.0742	1.0032	0.8894	0.7499	0.6643	0.5931
	0.2	1.0611	1.0026	0.9557	0.8402	0.7188	0.6233	0.5288
	0.3	1.0321	1.0041	0.9487	0.8276	0.7004	0.5761	0.4794
	0.4	1.0693	1.0912	1.0036	0.8822	0.7096	0.5721	0.4466
	0.5	1.2241	1.2744	1.1729	0.9997	0.7950	0.5879	0.4207
	0.6	1.5977	1.6504	1.5178	1.3002	1.0045	0.6862	0.4262
2.0	0.1	1.6090	1.5453	1.4268	1.2744	1.0706	0.9369	0.8268
	0.2	1.5239	1.4138	1.3219	1.1570	0.9845	0.8429	0.7167
	0.3	1.3948	1.3613	1.2719	1.1033	0.9224	0.7538	0.6230
	0.4	1.3089	1.4104	1.2916	1.1199	0.8962	0.7085	0.5492
	0.5	1.3556	1.5633	1.4297	1.2105	0.9497	0.6925	0.4893
	0.6	1.6600	1.9222	1.7566	1.4895	1.1360	0.7645	0.4662

Table 6 Normalised SIF under combined bending and torsion loadings, $F^{*}_{I,b\text{-}III,FE}$ obtained using finite element analysis

λ	a/D	a/b						
		0.0	0.2	0.4	0.6	0.8	1.0	1.2
0.5	0.1	0.9569	0.9217	0.8633	0.7719	0.7537	0.6690	0.5990
	0.2	0.9012	0.8762	0.8216	0.8036	0.6976	0.6026	0.5299
	0.3	0.9191	0.8988	0.8297	0.8005	0.6771	0.5644	0.4782
	0.4	1.0143	0.9856	0.9169	0.8006	0.6585	0.5227	0.4170
	0.5	1.2129	1.1833	1.0984	0.9488	0.7593	0.5665	0.4141
	0.6	1.6239	1.5825	1.4662	1.2607	0.9848	0.6860	0.4444
1.0	0.1	1.0735	1.0324	0.9641	0.8547	0.9914	0.8752	0.7795
	0.2	1.0008	0.9718	0.9089	1.0491	0.9041	0.7784	0.6817
	0.3	1.0066	0.9790	0.9040	1.0185	0.8566	0.7106	0.6040
	0.4	1.0906	1.0495	0.9812	0.8547	0.7042	0.5572	0.4444
	0.5	1.2812	1.2476	1.1558	0.9968	0.7950	0.5932	0.4373
	0.6	1.6860	1.6413	1.5185	1.3035	1.0160	0.7090	0.4606
2.0	0.1	1.4367	1.3900	1.2848	1.6330	1.6236	1.4250	1.2732
	0.2	1.3215	1.2885	1.1976	1.7097	1.4619	1.2554	1.0985
	0.3	1.2880	1.2543	1.1599	1.6117	1.3487	1.1195	0.9509
	0.4	1.3432	1.3082	1.2089	1.0454	0.8527	0.6775	0.5431
	0.5	1.5149	1.4731	1.3581	1.1649	0.9298	0.6947	0.5119
	0.6	1.9074	1.8549	1.7119	1.4592	1.1349	0.7916	0.5198

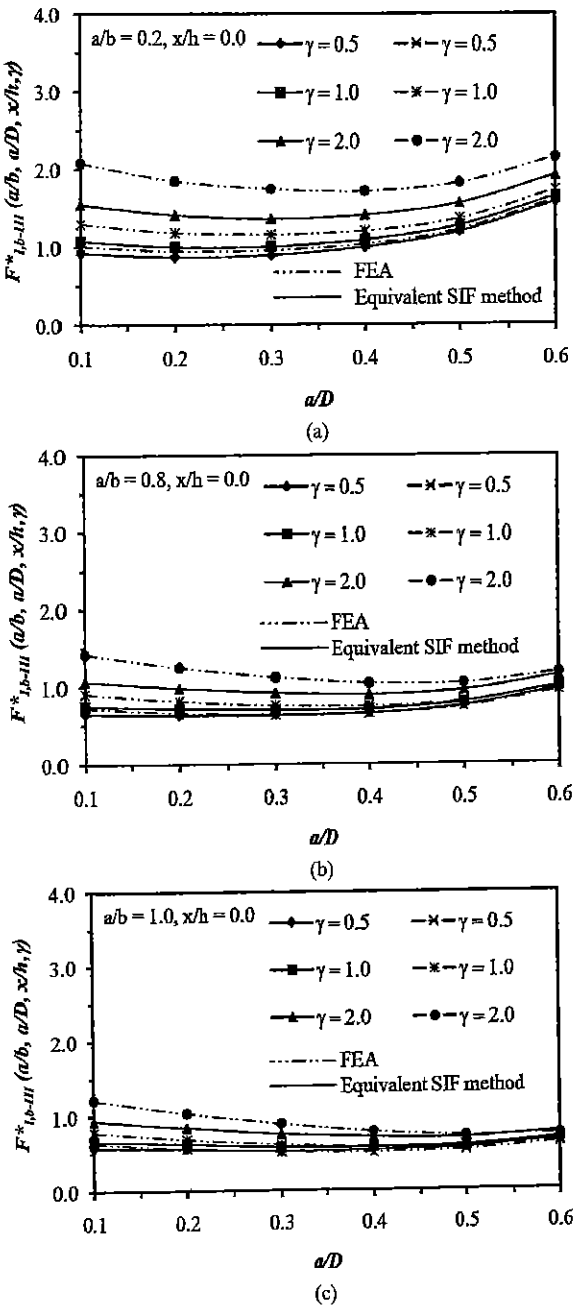

Fig. 14 Comparison of $F^*_{I,b\text{-}III}$ between two methods for (**a**) $a/b = 0.2$, (**b**) $a/b = 0.6$ and (**c**) $a/b = 1.0$ under bending and torsion loadings

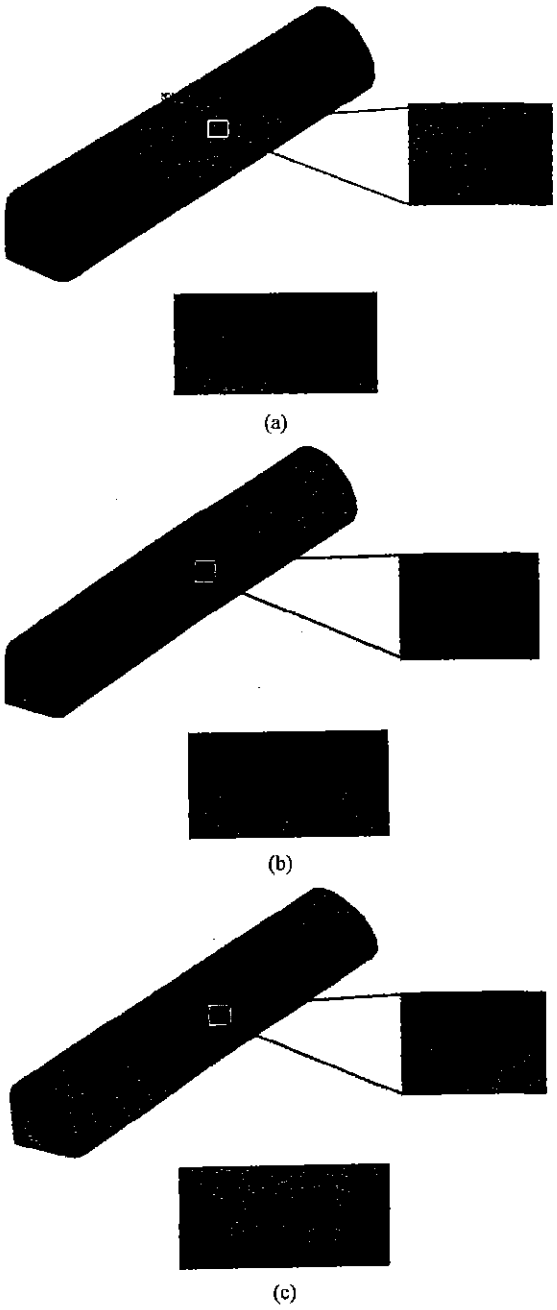

Fig. 15 Model deformations under (**a**) torsion, (**b**) tension and (**c**) combined torsion and tension loadings

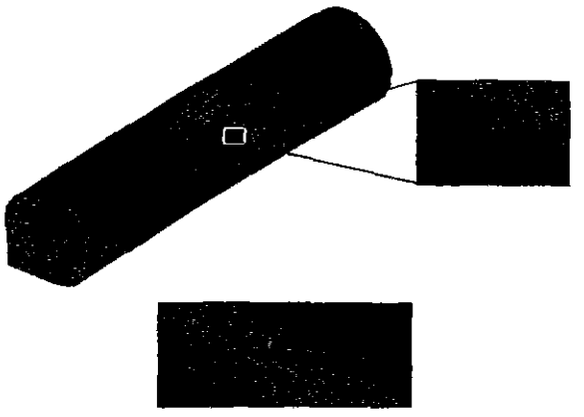

Fig. 16 Model deformations under bending moment

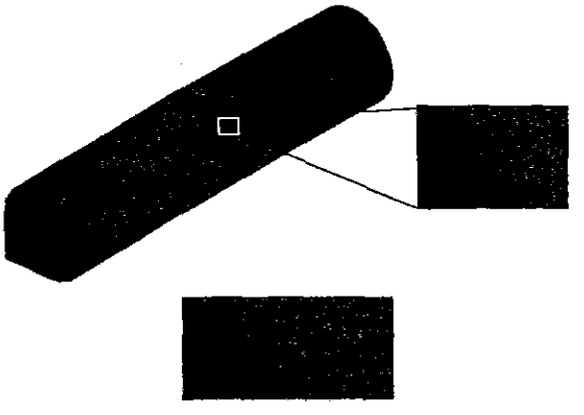

Fig. 17 Model deformations under combined bending and torsion loadings

closed under the pure torsion, and vice versa under the combined loadings. The opening of the crack faces under combined loadings increases the relative node distances and ANSYS then uses these relative distances to calculate the SIFs. As a result, higher F^*_{FE} is obtained with respect to the F^*_{EQ}, due to the different mechanisms of crack deformations and interactions.

References

1. Ismail AE, Ariffin AK, Abdullah S, Ghazali MJ (2011) Offset crack propagation analysis under mixed-mode loadings. Int J Automot Technol 12(2):225–232
2. Yan X, Liu B (2011) A numerical analysis of cracks emanating from a surface elliptical hole in infinite body in tension. Meccanica 46(2):263–278
3. Benedetti M, Beghini M, Bertini L, Fontanari V (2008) Experimental investigation on the propagation of fatigue cracks emanating from sharp notches. Meccanica 43(2):201–210
4. Mahmoud KM (2007) Fracture strength for a high strength steel bridge cable wire with a surface crack. Theor Appl Fract Mech 48(2):152–160
5. Gray GT, Thompson AW, William JC (1985) Influence of microstructure on fatigue crack initiation in fully pearlitic steels. Metall Trans 16(5):753–760
6. Lin XB, RA Smith (1997) Shape growth simulation of surface cracks in tension fatigue round bars. Int J Fatigue 19(6):461–469
7. Raju IS, Newman JC (1986) Stress intensity factors for circumferential surface cracks in pipes and rods under tension and bending loads. Fracture Mechanics: ASTM Special Technical Publication 905, No 17, pp 789–805
8. Murakami Y, Tsuru H (1987) Stress intensity factor handbook. Pergamon, New York
9. Carpinteri A (1992) Elliptical-arc surface cracks in round bars. Fatigue Fract Eng Mater Struct 15(11):1141–1153
10. Chue CH, Yeh CN (2011) Mode III fracture problem of two arbitrarily oriented cracks located within two bonded functionally graded material strips. Meccanica 46(2):447–469
11. Fonte MD, Freitas MD (1999) Stress intensity factor for semi-elliptical surface cracks in round bars under bending and torsion. Int J Fatigue 21(5):457–463
12. Shin CS, Cai CQ (2004) Experimental and finite element analyses on stress intensity factors of an elliptical surface crack in a circular shaft under tension and bending. Int J Fract 129(3):239–264
13. Carpinteri A, Brighenti R, Vantadori S (2006) Surface crack in notched round bars under cyclic tension and bending. Int J Fatigue 28(3):251–260
14. Carpinteri A, Vantadori S (2009) Sickle-shaped cracks in metallic round bars under cyclic eccentric axial loading. Int J Fatigue 31(4):759–765
15. Shahani AR, Habibi SE (2007) Stress intensity factors in a hollow cylinder containing a circumferential semi-elliptical crack subjected to combined loading. Int J Fatigue 29(1):128–140
16. Toribio J, Matos JC, Gonzalez B, Escuadra J (2009) Numerical modeling of crack shape evolution for surface flaws in round bars under tensile loading. Eng Fail Anal 16(2):618–630
17. Španiel M, Jurenka J, Kuželka J (2009) Verification of FE model of fatigue crack propagation under mixed mode conditions. Meccanica 44(1):189–195
18. Guinea GV, Planas J, Elices M (2000) K_I evaluation by the displacement extrapolation technique. Eng Fract Mech 66(3):243–255
19. Aslantas K (2003) A different approach for calculation of stress intensity factors in continuous fiber reinforced metal matrix composites. Int J Solids Struct 40(26):7475–7481
20. Aslantas K, Ergun E, Tasgetiren S (2006) A numerical model for calculation of stress intensity factors in particle-reinforced metal–matrix composites. Int J Mech Mater Des 3(2):201–208
21. Rice JR (1968) A path independent integral and the approximate analysis of strain concentration by notches and cracks. J Appl Mech 35:379–386

22. Kim YJ, Kim JS, Shim DJ, Kim YJ (2004) Applicability of reference stress based J estimates to semi-elliptical surface crack problems. J Strain Anal 39:245–260
23. Kim YJ, Shim DJ, Choi JB, Kim YJ (2002) Approximate J estimates for tension-loaded plates with semi-elliptical surface cracks. Eng Fract Mech 69:1447–1463
24. ANSYS 11.0 Documentation (2010). ANSYS Company
25. Ismail AE, Ariffin AK, Abdullah S, Ghazali MJ, Daud R (2011) Mode III stress intensity factor of surface crack in round bars. Adv Mater Res 214:192–196
26. Qian J, Fatemi A (1996) Mixed mode fatigue crack growth: A literature survey. Eng Fract Mech 55(6):969–990